J|A|C|S
ARTICLES
Published on Web 08/05/2003

Catalytic CO Oxidation by Free Au_2^-: Experiment and Theory

Liana D. Socaciu,[†] Jan Hagen,[†] Thorsten M. Bernhardt,*[,†] Ludger Wöste,[†] Ulrich Heiz,[‡] Hannu Häkkinen,[§] and Uzi Landman[§]

Contribution from the Institut für Experimentalphysik, Freie Universität Berlin, Arnimallee 14, D-14195 Berlin, Germany, Abteilung für Oberflächenchemie und Katalyse, Universität Ulm, D-89069 Ulm, Germany, and School of Physics, Georgia Institute of Technology, Atlanta, Georgia 30332-0430

Received July 30, 2002; E-mail: tbernhar@physik.fu-berlin.de

Abstract: Temperature-dependent rf-ion trap mass spectrometry and first-principles simulations reveal the detailed reaction mechanism of the catalytic gas-phase oxidation of CO by free Au_2^- ions in the presence of O_2. A metastable intermediate with a mass of $Au_2CO_3^-$ was observed at low temperatures. Two alternative structures corresponding to digold carbonate or peroxyformate are predicted for this intermediate. Both structures are characterized by low activation barriers for the formation of CO_2. These combined experimental and theoretical investigations provide a comprehensive understanding of the kinetics, energetics, and atomic arrangements along the reaction path, thus allowing a formulation of the catalytic cycle for the oxidation reaction.

Introduction

Until quite recently gold has not been considered relevant for the design of new materials for heterogeneous catalysis, because of its inert nature. However, reduction of the particle size to the nanoscale opened a new perspective on the catalytic propensities of gold. Indeed, during the past few years new catalysts based on highly dispersed nanoscale gold particles were developed which show superior performance to commonly employed materials in important catalytic reactions, such as CO oxidation and the partial oxidation of hydrocarbons, especially at low temperatures.[1,2] A detailed mechanistic understanding of this unique behavior is currently emerging, largely due to controlled UHV studies of model nanocatalysts as well as theoretical modeling and simulations. Most recently it was found that mass-selected deposited gold clusters Au_n^- ($n = 2-20$) on thin films of MgO(100) exhibit extremely sensitive size effects in the catalytic oxidation of CO. In particular, only clusters with eight or more atoms catalyze this reaction, and the CO_2 yield was found to exhibit a nonlinear dependence on cluster size for $n \geq 8$. A concurrent theoretical study revealed the importance of cluster charging by electron transfer from surface defects (oxygen vacancy F centers) of the MgO support.[3] In addition, a subsequent theoretical study predicted that even negatively charged free gold dimers, Au_2^-, are able to catalyze the gas-phase oxidation reaction of carbon monoxide to carbon dioxide in the presence of molecular oxygen.[4]

Motivated by this prediction we performed experiments in which mass-selected Au_2^- ions are exposed to a CO/O_2/He gas mixture inside an rf-octopole ion trap at a defined reaction temperature. These measurements provided evidence for catalytic CO_2 formation inside the ion trap. Furthermore, product ion analysis as a function of the reaction time, temperature, and reactive gas concentrations revealed the detailed kinetics of the catalytic reaction. On the basis of the observed kinetics, and in conjunction with first-principles theoretical calculations of the energetics and structures of the reaction intermediates along the reaction path, the mechanism of the catalytic reaction can be deduced. This is the first kinetic study on a catalytic metal cluster reaction and one of only a few examples where a full catalytic cycle has been demonstrated experimentally for gas-phase metal clusters.[5]

Experimental Procedure

The experimental setup consists of an octopole ion trap inserted into a multiple quadrupole mass spectrometer arrangement.[6] In brief, the gold cluster ions are sputtered from gold metal targets by a Cold Reflex Discharge Ion Source (CORDIS[7]). One particular cluster size is selected by a first quadrupole mass filter. Subsequently, the monodisperse cluster beam is thermalized by collisions with helium buffer gas prior to entering the ion trap. The octopole ion trap is prefilled with about 1 Pa partial pressure of helium buffer gas and a small, well-defined fraction of reactive gases (CO and O_2). The absolute pressure inside the trap is measured by a Baratron gauge (MKS, Typ 627B). The ion trap assembly is attached to a helium cryostat, allowing variable temperature

[†] Freie Universität Berlin.
[‡] Universität Ulm.
[§] Georgia Institute of Technology.

(1) Haruta, M. *Catal. Today* **1997**, *36*, 153. Haruta, M. *Appl. Catal. A* **2001**, *222*, 427.
(2) Häkkinen, H.; Abbet, S.; Sanchez, A.; Heiz, U.; Landman, U. *Angew. Chem., Int. Ed.* **2003**, *42*, 1297.
(3) Sanchez, A.; Abbet, S.; Heiz, U.; Schneider, W.-D.; Häkkinen, H.; Barnett, R. N.; Landmann, U. *J. Phys. Chem. A* **1999**, *103*, 9573.
(4) Häkkinen, H.; Landman, U. *J. Am. Chem. Soc.* **2001**, *123*, 9704.
(5) Schnabel, P.; Weil, K. G.; Irion, M. P. *Angew. Chem., Int. Ed. Engl.* **1992**, *31*, 636. Shi, Y.; Ervin, K. M. *J. Chem. Phys.* **1998**, *108*, 1757. Ervin, K. M. *Int. Rev. Phys. Chem.* **2001**, *20*, 127.
(6) Socaciu, L. D.; Hagen, J.; Heiz, U.; Bernhardt, T. M.; Leisner, T.; Wöste, L. *Chem. Phys. Lett.* **2001**, *340*, 282.
(7) Keller, R.; Nöhmeier, F.; Spädtke, P.; Schönenberg, M. H. *Vacuum* **1984**, *34*, 31.

10.1021/ja027926m CCC: $25.00 © 2003 American Chemical Society

adjustment in the range between 20 and 350 K. Thermal equilibration of the clusters entering the trap is achieved within a few thousand collisions with the buffer gas, i.e., in a few milliseconds under our operating conditions.[8] The cluster ions are stored in the trap for a considerably longer time period, typically for several seconds, without significant ion loss. The trap is filled with gold cluster anions up to the space charge limit, i.e., about 10^4 ions per mm^3. After the chosen reaction time, all ions, reactants, intermediates, and products are extracted by applying an electrostatic field, and the ion distribution is analyzed via a second quadrupole mass spectrometer. By recording all ion concentrations as a function of the reaction time, the kinetics of the reaction may be obtained. The ion trap operates in the kinetic low-pressure regime, which means that a Lindemann-type mechanism has to be considered for each reaction step and that the rate depends on the buffer gas pressure.[9] Since the concentrations of the reactive gases and the buffer gas in the octopole trap are orders of magnitude higher than the Au_2^- concentration, these concentrations are considered to remain constant in the kinetic evaluation procedure.[9] Hence, all the proposed reaction steps are assumed to follow pseudo-first-order kinetics. Possible reaction mechanisms are evaluated by fitting the integrated rate equations to the experimental kinetic data. The integration of the rate equations is performed numerically by using the fourth-order Runge−Kutta algorithm. The employed fitting procedure consists of an iterative nonlinear least-squares method.[10] Our method is the basic approach to macroscopic chemical kinetics[9] and results in an optimized kinetic model presenting the most simple reaction mechanism with the best fit to the experimental data. Note that in this approach more complex mechanisms which result in the same fit quality are discarded. Thus, the obtained reaction steps are not necessarily elementary reaction steps. Benson's rule of chemical kinetics[9] applies to all deduced reaction mechanisms.

Computational Method

The interaction of Au_2^- with CO and O_2 as well as the complete catalytic cycle was investigated via density functional theory. The Kohn−Sham (KS) equations were solved using the Born−Oppenheimer (BO) local-spin-density (LSD) molecular dynamics (MD) method (BO-LSD-MD),[11] including generalized gradient corrections (GGA),[12] with nonlocal norm-conserving pseudopotentials[13] for the $5d^{10}\,6s^1$, $2s^2\,2p^2$, and $2s^2\,2p^4$ valence electrons of the Au, C, and O atoms, respectively. Relativistic effects[14] are prominent in gold clusters,[15] and we have used here a scalar-relativistic treatment of the pseudopotential[16] which has been verified to yield results in close agreement with a full relativistic approach.[17]

The BO-LSD-MD method is particularly suited for this study, since it does not employ periodic replication of the ionic system (that is, no supercell is used), thus allowing accurate calculations on both neutral and charged systems.[11] Our calculations give an accurate description of the bonding properties of neutral and anionic dimers of Au_2 and AuO as well as those of CO, O_2, and CO_2 molecules.[4] All the structures shown here are obtained via unconstrained optimizations of the spatial atomic arrangements and of the spin configurations.

In our investigation of the reactions paths we determined several reaction barriers for the formation of intermediate complexes as well as for the formation and release of CO_2. The reaction barriers were obtained by constrained optimizations, where the reaction coordinate x_R (e.g., the distance between judiciously chosen atoms, or between an approaching atom and the center of mass of another group of atoms, etc.), was varied by increments of 0.1−0.2 Å, with all other degrees of freedom fully relaxed for each value of x_R. This procedure yields the shape of the reaction barrier along the reaction path, and with the discretization of x_R used here the barrier height (and the transition state) is estimated within 0.1 eV. In certain cases the connectivity between the transition state and the product was verified using first-principles dynamical simulations, releasing the system from the transition state.

Results and Discussion

Experimental. First, we investigated the reactivity of Au_2^- separately toward O_2 or CO. In agreement with previous recent studies no reaction with CO was observed at room temperature, while $Au_2O_2^-$ was the only product in the reaction with O_2.[18,19] The product ion concentrations as a function of the reaction time t_R for the reaction with O_2 are displayed in Figure 1a. The kinetics can best be fitted by a straightforward association reaction mechanism:

$$Au_2^- + O_2 \rightarrow Au_2O_2^- \tag{1a}$$

The solid lines in Figure 1a represent the fitted integrated rate equations for this mechanism. As explained in the Experimental Procedure, our experiment operates in the kinetic low-pressure regime, therefore the obtained pseudo-first-order rate constant k contains the termolecular rate constant $k^{(3)}$ as well as the concentrations of the helium buffer gas and of the reactant:

$$k = k^{(3)}[\mathrm{He}][O_2] \tag{1b}$$

The details of the reaction are described by the Lindemann energy transfer model for association reactions which is represented by the following equations:[9]

$$Au_2^- + O_2 \rightleftarrows Au_2O_2^-{}^* \tag{1c}$$

$$Au_2O_2^-{}^* + \mathrm{He} \rightarrow Au_2O_2^- + \mathrm{He}^* \tag{1d}$$

The intermediate, energetically excited ion−molecule complex $Au_2O_2^-{}^*$ can decompose back to the reactants, if no stabilizing collisions with a background helium atom take place. For each similar reaction step identified in the kinetic evaluation and fitting procedure, such a Lindemann-type reaction scheme has to be considered as elementary reaction scenario.

Next, partial pressures of both reaction gases, O_2 and CO, were introduced into the ion trap. This changes the kinetics of

(8) Westergren, J.; Grönbeck, H.; Kim, S.-G.; Tománek, D. *J. Chem. Phys.* **1997**, *107*, 3071. Westergren, J.; Grönbeck, H.; Rosén, A.; Nordholm, S. *J. Chem. Phys.* **1998**, *109*, 9848. Hess, H.; Kwiet, S.; Socaciu, L.; Wolf, S.; Leisner, T.; Wöste, L. *Appl. Phys. B* **2000**, *71*, 337.
(9) Steinfeld, J. I.; Francisco, J. S.; Hase, W. L. *Chemical Kinetics and Dynamics*, 2nd ed.; Prentice Hall: Upper Saddle River, NJ, 1999. Laidler, K. J. *Chemical Kinetics*, 3rd ed.; HarperCollins: New York, 1987.
(10) IBM. *Chemical Kinetics Simulator*, 1.0 ed.; IBM Corporation: 1995. Schumacher, E. *DETMECH−Chemical Reaction Kinetics Software*; University of Bern: Chemistry Departement, 1997 (http://iacrs1.unibe.ch/~chemsoft/).
(11) Barnett, R. N.; Landman, U. *Phys. Rev. B* **1993**, *48*, 2081. This method does not use periodic boundary conditions for the ionic system.
(12) Perdew, J. P.; Burke, K.; Ernzerhof, M. *Phys. Rev. Lett.* **1996**, *77*, 3865.
(13) Troullier, N.; Martins, J. L. *Phys. Rev. B* **1991**, *43*, 1993. The core radii (in a_0) are as follows: Au: s(2.50), p(3.00), d(2.00); C: s(1.50), p(1.54); O: s(1.45), p(1.45), with Au(s), C(p), and O(p) as local components. The Kohn−Sham orbitals are expanded in a plane-wave basis with 62 Ry energy cutoff.
(14) Pyykkö, P. *Chem. Rev.* **1988**, *88*, 563.
(15) Häkkinen, H.; Moseler, M.; Landman, U. *Phys. Rev. Lett.* **2002**, *89*, 033401.
(16) Kleinman, L. *Phys. Rev. B* **180**, *21*, 2630. Bachelet, G. B.; Schluter, M. *Phys. Rev. B* **1982**, *25*, 2103.
(17) Häkkinen, H.; Landman, U. *Phys. Rev. B* **2000**, *62*, R2287. Varga, S.; Bolton, K.; Grönbeck, H.; Snis, A.; Rosén, A.; Fricke, B. *Eur. J. Phys. D* **2001**, *16*, 29.
(18) Cox, D. M.; Brickman, R.; Creegan, K.; Kaldor, A. *Z. Phys. D* **1991**, *19*, 353. Lee, T. H.; Ervin, K. M. *J. Phys. Chem.* **1994**, *98*, 10023. Salisbury, B. E.; Wallace, W. T.; Whetten, R. L. *Chem. Phys.* **2000**, *262*, 131. Wallace, W. T.; Whetten, R. L. *J. Phys. Chem. B* **2000**, *104*, 10964.
(19) Hagen, J.; Socaciu, L. D.; Heiz, U.; Bernhardt, T. M.; Wöste, L. *Eur. J. Phys. D*, in press.

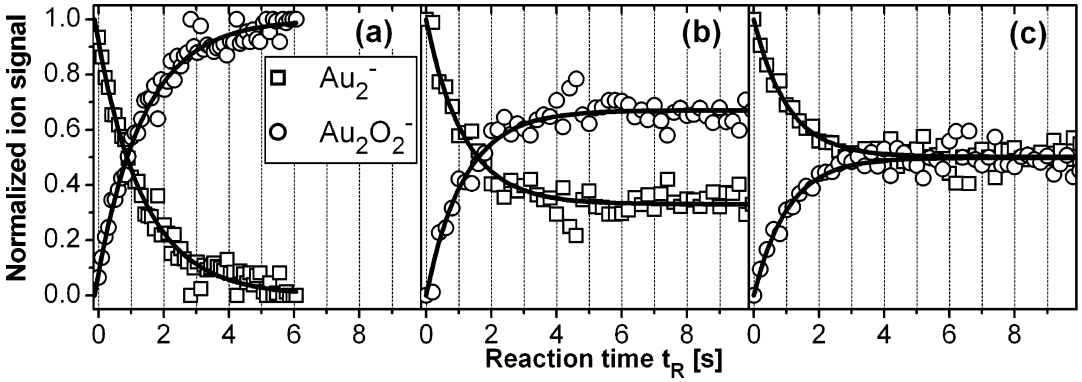

Figure 1. Concentration of all product ions observed during Au_2^- reaction inside the octopole ion trap as a function of the reaction time t_R for different CO partial pressures: (a) no CO in the trap, $p(CO) = 0$; (b) $p(CO) = p(O_2)$; (c) $p(CO) = 2p(O_2)$. Reaction temperature $T_R = 300$ K; $p(O_2) = 0.12$ Pa; $p(He) = 1.2$ Pa. The open symbols represent the experimental data, normalized to the initial Au_2^- concentration and to the total ion concentration in the trap. The solid lines are obtained by fitting the integrated rate equations of the proposed reaction mechanisms to the experimental data ((a) mechanism equation 1a; (b), (c) mechanism equation 2, see text).

the reaction with Au_2^- drastically. We will start to discuss the observed ions and kinetics at room temperature before presenting the temperature-dependent investigations that lead to the observation of a reaction intermediate and the inference of a full catalytic cycle. The room-temperature kinetics are displayed in Figures 1b and 1c for different O_2/CO pressure ratios. No further product ions besides $Au_2O_2^-$ are detected. However, an offset in the Au_2^- signal is observed at long reaction times, indicating a more complex reaction mechanism. The simplest reaction mechanism that is able to fit the experimental data is an equilibrium reaction:

$$Au_2^- + O_2 \underset{k_{-1}}{\overset{k_1}{\rightleftharpoons}} Au_2O_2^- \qquad (2)$$

Here k_1 and k_{-1} are the rate constants for the forward and backward reactions, respectively. Note that the Au_2^- offset is only observed when CO is present in the ion trap, although this is not reflected in eq 2. The influence of the CO concentration on the Au_2^- offset, i.e., the equilibrium concentration of Au_2^-, can be seen from a comparison of the kinetic traces in Figures 1b and 1c: In Figure 1b, the ratio $p(CO)/p(O_2) = 1$, compared to $p(CO)/p(O_2) = 2$ in Figure 1c. Correlated with this, the rate constant k_{-1} (eq 2) doubles in Figure 1c compared to that in Figure 1b. Hence, increasing the CO partial pressure enhances the backward reaction step. Consequently, the above indicates that eq 2 fails to provide a complete description of the reaction and that an appropriate description involves more complex reaction steps.

To obtain further insight into the mechanism of this reaction, we recorded the reaction products as a function of the reaction temperature. Figure 2a shows a mass spectrum of the product ion distribution under room-temperature conditions with both reactive gases present in the trap. Au_2^- and $Au_2O_2^-$ are the only ions detected. Cooling the ion trap down below room temperature surprisingly revealed the appearance of an additional signal. Figure 2b displays the corresponding mass spectrum at 100 K. The new ion signal emerges at the mass assigned to the species with a stoichiometry of $Au_2(CO)O_2^-$. Obviously, at lower temperatures we were able to isolate an intermediate product of the reaction mechanism. The ion stoichiometry clearly shows that CO and O_2 are able to coadsorb on an Au_2^- dimer,

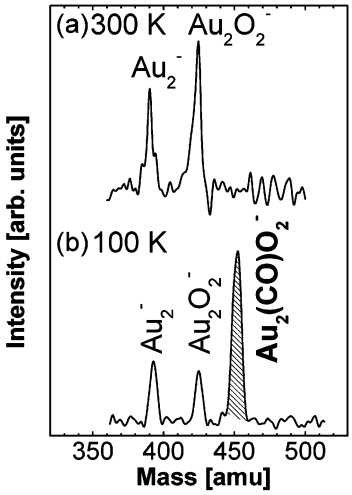

Figure 2. Mass spectra of product ion distributions analyzed after trapping Au_2^- for 500 ms inside the octopole ion trap filled with 0.02 Pa O_2, 0.05 Pa CO, and 1.23 Pa He. (a) At a reaction temperature of 300 K only Au_2^- and $Au_2O_2^-$ are detected. Cooling down reveals an additional ion signal appearing at the mass of $Au_2(CO)O_2^-$. Mass spectrum (b) shows the ion distribution at 100 K.

and this complex represents a key step in the path toward catalytic CO oxidation to CO_2 as has been predicted in an earlier theoretical study[4] (the preferred tendency of small gold cluster anions to coadsorb CO and O_2 molecules could be confirmed experimentally for the gold trimer as well,[20] and also recently[21] for larger Au_n^-).

Having identified this reaction intermediate, we monitored the concentrations of all ions observed (Au_2^-, $Au_2O_2^-$, and $Au_2(CO)O_2^-$) as a function of the reaction time, under a multitude of different reaction conditions. The dependencies of the kinetics on the variation of the different reaction parameters (reaction temperature T_R, CO partial pressure $p(CO)$, O_2 partial pressure $p(O_2)$) were investigated. The aim of this exploration was to find a reaction mechanism that fits all the obtained data, as well as one that is in accord with the room-temperature kinetics represented in Figures 1b and 1c. The most simple reaction mechanism that fulfills these prerequisites, and fits all the kinetic data measured under all the different reaction

(20) Hagen, J.; Socaciu, L. D.; Elijazyfer, M.; Heiz, U.; Bernhardt, T. M.; Wöste, L. *Phys. Chem. Chem. Phys.* **2002**, *4*, 1707.
(21) Wallace, W. T.; Whetten, R. L. *J. Am. Chem. Soc.* **2002**, *124*, 7499.

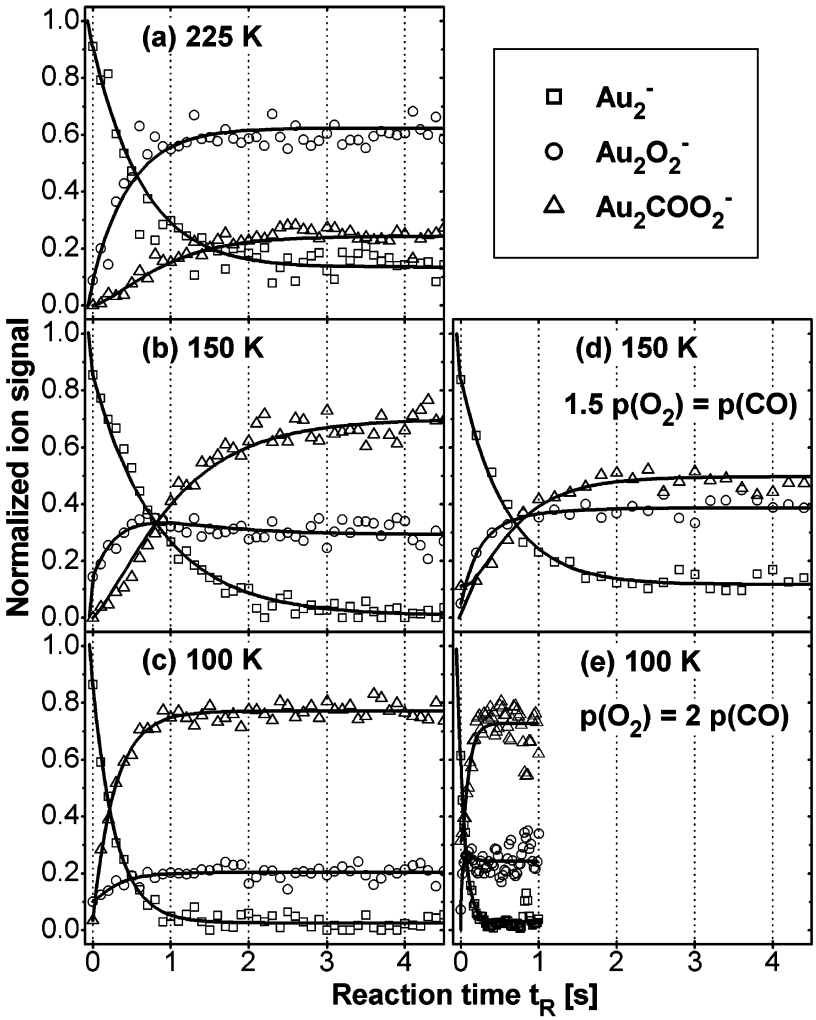

Figure 3. Product ion concentrations as a function of the reaction time for three different reaction temperatures and different reactant gas concentrations. (a) $T_R = 225$ K; $p(O_2) = 0.09$ Pa; $p(CO) = 0.10$ Pa; $p(He) = 1.07$ Pa. (b) $T_R = 150$ K; $p(O_2) = 0.04$ Pa; $p(CO) = 0.04$ Pa; $p(He) = 1.0$ Pa. (c) $T_R = 100$ K; $p(O_2) = 0.02$ Pa; $p(CO) = 0.03$ Pa; $p(He) = 1.0$ Pa. (d) $T_R = 150$ K; $p(O_2) = 0.04$ Pa; $p(CO) = 0.06$ Pa; $p(He) = 1.01$ Pa. (e) $T_R = 100$ K; $p(O_2) = 0.08$ Pa; $p(CO) = 0.04$ Pa; $p(He) = 1.03$ Pa. Open symbols represent the normalized experimental data. The solid lines are obtained by fitting the integrated rate equations of the catalytic reaction cycle (eq 3) to the experimental data. Note that the reactant gas concentrations in (a)−(c) were kept constant and equal for the different temperatures within the error limits of our experiment (±0.008 Pa). The helium concentration could not be maintained constant for the different temperatures due to the limited pressure range for ion trapping.

conditions, is described by the reaction equations given below:

$$Au_2^- + O_2 \xrightarrow{k_1} Au_2O_2^- \quad (3a)$$

$$Au_2O_2^- + CO \underset{k_{-2}}{\overset{k_2}{\rightleftharpoons}} Au_2(CO)O_2^- \quad (3b)$$

$$Au_2(CO)O_2^- + CO \xrightarrow{k_3} Au_2^- + 2CO_2 \quad (3c)$$

Kinetic traces of the catalytic reaction at three different reaction temperatures as well as at different O_2 and CO partial pressures are shown in Figure 3. The fit of the integrated rate equations of this mechanism (eqs 3) is represented by the solid lines. As can be seen from the graphs in Figure 3, an excellent agreement with all the measured kinetic data has been achieved. It should be noted that the quality of the fit is very sensitive to the postulated reaction steps and that the kinetic evaluation procedure that we have employed is clearly able to discriminate against alternative mechanisms, as has been demonstrated before.[6,9] The replacement of the equilibrium in reaction 3b, e.g., by a simple forward reaction will lead to a mechanism that yields an inadequate fit to the experimental data. The $Au_2O_2^-$ signal will then disappear at long reaction times, which is not the case as can be seen from Figure 3.

Figures 3d−e show examples of the dependence of the reaction kinetics on the reactant partial pressures. The dependence of a pseudo-first-order rate constant on the concentration of a reactant (O_2 or CO) demonstrates the involvement of the reactant in this particular reaction step (cf. eq 1b and Table 1). A set of pseudo-first-order rate constants for the mechanism equations 3 obtained for different experimental conditions is listed in Table 1. The shown error values of k_1 and k_2 are mainly due to the error in the partial pressures. For k_{-2} and k_3 the possible variation of the rate constants resulting in the same fit quality is larger than the partial pressure uncertainty and thus determines the error bars of the rates in these cases. Figures 4 and 5 show graphical representations of this data set. In the following we will discuss in detail some important implications of reaction mechanism equations 3 based on these results:

Table 1. Pseudo-First-Order Rate Constants Obtained by Fitting the Reaction Mechanism Equations 3 to the Kinetic Data under Various Experimental Conditions

T [K]	$p(O_2)$ [Pa]	p(CO) [Pa]	p(He) [Pa]	k_1 [s^{-1}]	k_2 [s^{-1}]	k_{-2} [s^{-1}]	k_3 [s^{-1}]
100	0.02	0.03	1.01	3 ± 2	38 ± 10	10 ± 2	0.10 ± 0.09
	0.04	0.04	1.03	6 ± 2	46 ± 9	11 ± 3	0.30 ± 0.15
	0.04	0.08	1.02	8 ± 2	77 ± 8	30 ± 6	0.55 ± 0.25
	0.08	0.04	1.03	13 ± 2	27 ± 6	8 ± 2	0.40 ± 0.20
150	0.04	0.04	1.00	1.2 ± 0.3	1.9 ± 0.4	0.8 ± 0.2	0.05 ± 0.04
	0.04	0.06	1.00	1.5 ± 0.3	3.0 ± 0.4	2.0 ± 0.4	0.35 ± 0.15
	0.04	0.16	1.00	2.2 ± 0.5	14.4 ± 0.8	23 ± 5	0.65 ± 0.15
	0.06	0.07	1.03	3.7 ± 0.5	7.0 ± 0.8	2.5 ± 0.5	0.45 ± 0.15
	0.06	0.11	1.05	3.9 ± 0.5	14 ± 1	10 ± 2	0.55 ± 0.15
	0.12	0.05	1.04	4.3 ± 0.3	3.0 ± 0.5	1.8 ± 0.4	0.65 ± 0.15
190	0.07	0.07	1.05	1.8 ± 0.2	2.4 ± 0.3	0.5 ± 0.1	0.30 ± 0.10
	0.08	0.16	1.04	2.2 ± 0.3	4.0 ± 0.2	2.4 ± 0.5	0.45 ± 0.15
	0.15	0.08	1.04	3.1 ± 0.2	3.2 ± 0.4	1.7 ± 0.4	0.30 ± 0.10
225	0.09	0.10	1.07	1.5 ± 0.2	0.84 ± 0.07	1.4 ± 0.3	0.80 ± 0.40
300[a]	0.13	0.13	1.05	0.94 ± 0.06	0.34 ± 0.02	<0.1	>10
	0.13	0.26	1.05	0.94 ± 0.06	0.67 ± 0.02	<0.1	>10
	0.26	0.13	1.05	1.61 ± 0.05	0.44 ± 0.03	<0.1	>10

[a] Note that at 300 K no intermediate product is observed. To be able to fit reaction mechanism equations 3 in this case, an intermediate product concentration below the detection limit of the experiment is assumed.

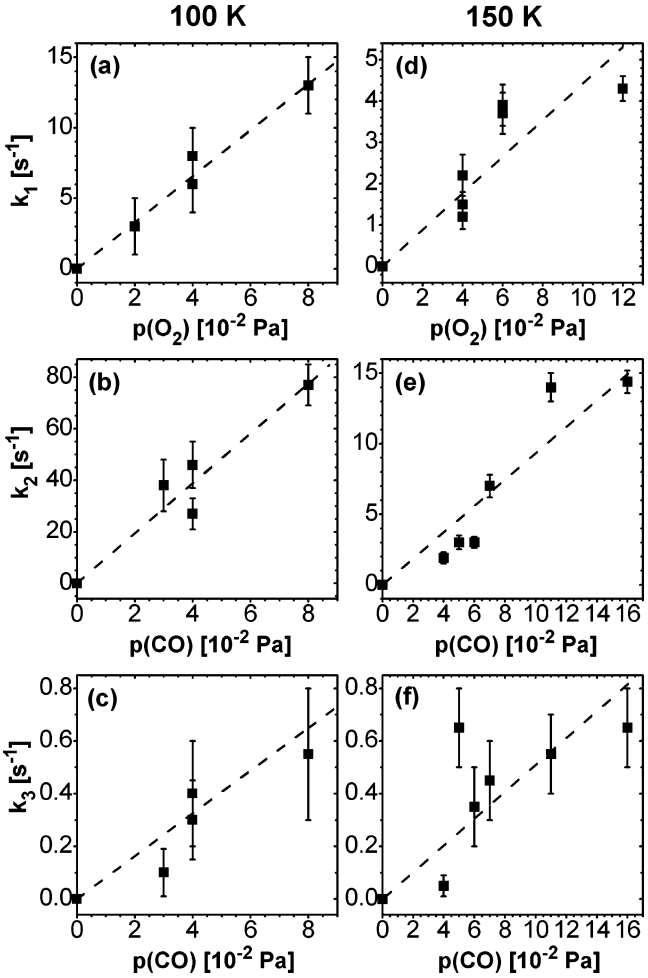

Figure 4. Reactant partial pressure dependence of rate constants k_n at 100 K (a−c) and 150 K (d−f). (a) and (d) show the O_2 partial pressure dependence of k_1. (b,e) and (c,f) show the CO partial pressure dependences of k_2 and k_3, respectively. The dashed lines represent linear fits to the data and are drawn as guide to the eye.

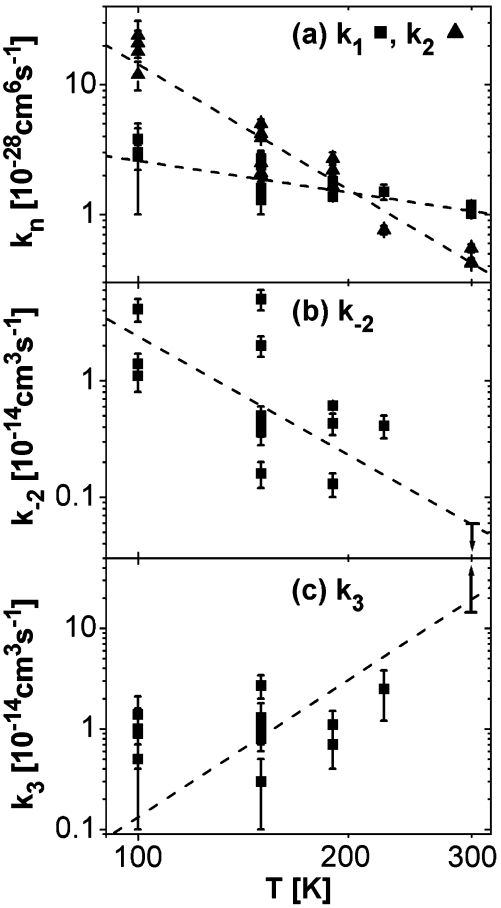

Figure 5. Temperature dependence of the rate constants of reaction mechanism equations 3 (cf. Table 2) in double logarithmic representation. (a) Termolecular rate constants k_1 and k_2. (b) Bimolecular rate constant k_{-2}. (c) Bimolecular rate constant k_3. Dashed lines are drawn as a guide to the eye.

(1) The mechanism reveals that O_2 adsorption precedes CO adsorption in the catalytic reaction. This is further supported by the fact that no signal for the ion Au_2CO^- is observed and by the reaction kinetics of Au_2^- when only O_2 or CO are present in the trap; the adsorption of O_2 is by about an order of magnitude faster than the adsorption of CO molecules.[19]

(2) Varying the oxygen partial pressure inside the trap affects the rate constant k_1 as can be seen from Table 1. In fact, all other rate constants remain unaffected by the variation of $p(O_2)$ within the confidence limits of the data (cf. Table 1). From

Table 2. Termolecular Rate Constants $k_1^{(3)}$ and $k_2^{(3)}$, as Well as Bimolecular Rate Constants $k_{-2}^{(2)}$ and $k_3^{(2)}$ Deduced from the Pseudo-First-Order Values in Table 1[a]

T [K]	$p(O_2)$ [Pa]	p(CO) [Pa]	p(He) [Pa]	$k_1^{(3)}$ [10^{-28} cm^6 s^{-1}]	$k_2^{(3)}$ [10^{-28} cm^6 s^{-1}]	$k_{-2}^{(2)}$ [10^{-14} cm^3 s^{-1}]	$k_3^{(2)}$ [10^{-14} cm^3 s^{-1}]
100	0.02	0.03	1.01	3 ± 2	24 ± 7	1.4 ± 0.3	0.5 ± 0.4
	0.04	0.04	1.03	2.8 ± 0.6	21 ± 5	1.4 ± 0.3	1.0 ± 0.6
	0.04	0.08	1.02	3.8 ± 0.8	18 ± 2	4.1 ± 0.9	0.9 ± 0.5
	0.08	0.04	1.03	2.9 ± 0.3	12 ± 3	1.1 ± 0.3	1.4 ± 0.7
150	0.04	0.04	1.00	1.3 ± 0.3	2.0 ± 0.4	0.16 ± 0.04	0.3 ± 0.2
	0.04	0.06	1.00	1.6 ± 0.4	2.1 ± 0.3	0.41 ± 0.08	1.2 ± 0.6
	0.04	0.16	1.00	2.4 ± 0.5	3.9 ± 0.2	5 ± 1	0.8 ± 0.2
	0.06	0.07	1.03	2.6 ± 0.4	4.2 ± 0.5	0.5 ± 0.1	1.3 ± 0.5
	0.06	0.11	1.05	2.7 ± 0.4	5.0 ± 0.4	2.0 ± 0.4	1.0 ± 0.3
	0.12	0.05	1.04	1.5 ± 0.1	2.5 ± 0.4	0.36 ± 0.08	2.7 ± 0.7
190	0.07	0.07	1.05	1.7 ± 0.2	2.2 ± 0.3	0.13 ± 0.03	1.1 ± 0.4
	0.08	0.16	1.04	1.8 ± 0.2	1.65 ± 0.09	0.61 ± 0.02	0.7 ± 0.3
	0.15	0.08	1.04	1.37 ± 0.08	2.7 ± 0.3	0.43 ± 0.09	1.1 ± 0.4
225	0.09	0.10	1.07	1.5 ± 0.2	0.76 ± 0.06	0.41 ± 0.09	2.5 ± 1.3
300	0.13	0.13	1.05	1.18 ± 0.08	0.43 ± 0.03	<0.04	>32
	0.13	0.26	1.05	1.18 ± 0.08	0.42 ± 0.02	<0.04	>16
	0.26	0.13	1.05	1.01 ± 0.04	0.55 ± 0.04	<0.04	>32

[a] Note that deviations at high p(CO) are due to side reaction effects (see also text).

Figures 4a and d it can be seen that k_1 rises linearly with increasing $p(O_2)$ as expected.

(3) An increase in the carbon monoxide partial pressure results at room temperature in an increasing back reaction rate k_{-1} in eq 2, i.e., the Au_2^- offset (the Au_2^- equilibrium concentration) is increasing, as can be seen from the Figures 1b and 1c. Resolving the kinetics at lower temperatures also reveals an increase of the Au_2^- offset with increasing p(CO) (Figures 3b and d). This is reflected in the fact that both, k_2 and k_3 (in eqs 3), increase at larger p(CO) as illustrated in Figures 4b−c at 100 K as well as in Figures 4e−f at 150 K. The relation between k_{-2} (eq 3b) and p(CO) is more complicated. In particular, it appears that at higher CO partial pressures and low temperatures CO adsorption starts to compete with O_2 adsorption in the first reaction step. This leads to the observed systematic increase of k_1 with p(CO) at lower temperatures (cf. Table 1). From this side reaction, a new product, $Au_2(CO)O_2^-$, with a structure different than that of the discussed intermediate in eqs 3 will form, competing with the catalytic cycle. The observed large increase of k_{-2} at higher p(CO) (cf. Table 1) can be assigned to the decomposition of this structurally different intermediate resulting from first CO and then O_2 adsorption.

(4) As the experiment is conducted in the kinetic low-pressure regime, stabilizing or activating collisions have to be considered in the elementary reaction steps according to the Lindemann model. Hence, the elementary reaction steps of reaction equation 3a are considered to be equal to those of eqs 1c−d. The same is true for the forward reaction step (k_2) of reaction equation 3b. For the backward reaction step (k_{-2}) of reaction equation 3b, a Lindemann mechanism for unimolecular decompositions has to be considered,[9] resulting in an overall bimolecular rate constant. Reaction equation 3c represents a bimolecular reaction with more than one product (no association reaction), and no further intermediates could be identified. Therefore, the involvement of a He collision in the elementary reaction scenario is not required. In particular, in this reaction step (eq 3c), the first-principles calculations described in the following section help to provide insight into the structure and energetics along the reaction path on a molecular basis.

(5) As discussed above, the postulation of an equilibrium in step 3b is essential to the reaction mechanism. This in turn has implications on the possible structure of the intermediate species $Au_2(CO)O_2^-$ in the catalytic cycle equations 3 which might be a simple co-adsorption of the two molecules, e.g., on different sides of Au_2^-, or already a reacted carbonate (CO_3)-like species adsorbed onto the gold dimer (see also Theoretical section). Apparently, the observed intermediate can have different isomers and one of them is formed by molecular coadsorption of CO and O_2, because otherwise the possible CO loss required by eq 3b would not be feasible.

(6) Further insight into this issue and the reaction energetics can be gained from temperature-dependent measurements as shown in Figure 3a−c. We observe that with decreasing temperature the final equilibrium concentration of $Au_2(CO)O_2^-$ increases, whereas the offset in the Au_2^- concentration as well as the $Au_2O_2^-$ concentration decrease. This is reflected in the different termolecular and bimolecular rate constants as a function of reaction temperature, which are listed in Table 2. The values are calculated from the pseudo-first-order rates in Table 1. Figure 5 presents plots of the rate constants as a function of temperature. In general, good agreement is obtained for the bi- and termolecular rate constants measured at the same temperature but different reactant gas concentrations, as expected. Deviations are observed at high CO partial pressures, in particular for the rate constants $k_1^{(3)}$ and $k_{-2}^{(2)}$. These deviations can be understood by considering the influence of the side reaction introduced above which is in competition with the catalytic cycle at high p(CO). From Figure 5a it can be seen that the rate constants $k_1^{(3)}$ and $k_2^{(3)}$ decrease with increasing temperature. This negative temperature dependence is indicative of a barrierless reaction and can be explained in the framework of the Lindemann theory.[9,19] Most importantly, however, $k_3^{(2)}$ increases with increasing temperature (Figure 5c). Hence, an activation barrier is involved in reaction step 3c. This corresponds to the increasing $Au_2(CO)O_2^-$ signal and the decreasing Au_2^- offset with decreasing temperature and agrees well with our theoretical calculations as will be discussed below. The case of $k_{-2}^{(2)}$ is again more complicated: As the forward reaction of eq 3b (k_2) has been identified to be barrierless, an activation barrier and thus a positive temperature dependence of $k_{-2}^{(2)}$ would be expected for the back reaction step of reaction 3b. However, from Figure 3b a negative trend of the temperature

dependence of $k_{-2}^{(2)}$ is detected. This observation also points toward the participation of different isomers of the intermediate in the catalytic cycle equations 3. At room temperature, the most stable isomers, such as the carbonate structure (cf. Theoretical part), are populated, but do not dissociate back to $Au_2O_2^-$. More weakly bound isomers that are able to redissociate are preferably populated at lower temperatures. The relative concentration of stable and weakly bound, dissociating isomers gives rise to the observed negative temperature dependence of $k_{-2}^{(2)}$. Possible structures of the intermediate $Au_2(CO)O_2^-$ will be presented in the Theoretical section.

(7) Finally, from the kinetic traces of the room-temperature catalytic reaction in Figure 1c, we calculated the catalytic turnover-frequency (TOF) to be 0.5 CO_2 molecules per gold cluster per second. This is in the same order of magnitude as the catalytic activity of oxide-supported gold cluster particles with a size of a few nanometers, which ranges between 0.2 s^{-1} per Au atom (~2 nm diameter particles at 273 K) and 4 s^{-1} per Au atom (3.5 nm particles at 350 K).[1,22]

Theoretical. The interaction and bonding of Au_2^- with O_2 and CO has been discussed by some of us before.[4] In the optimal configuration O_2 is bonded to Au_2^- end-on (i.e. a planar [Au−Au−O−O]$^-$ configuration), with interatomic distances of d(Au−Au) = 2.58 Å, d(Au−O) = 2.11 Å, d(O−O) = 1.34 Å, and angles ∠(Au−O−O) = 115.6° and ∠(Au−Au−O) = 180°. The bonding mechanism involves partial electron transfer (0.4 e) from the metal cluster to the antibonding π-orbital of the oxygen molecule, making the oxygen molecule a superoxo-like species. The binding energy is 1.39 eV, and molecular adsorption is energetically favored over dissociative adsorption. Furthermore, the molecular binding is a nonactivated process, i.e., a barrierless reaction channel exists for the approaching oxygen molecule leading to the adsorption configuration described above. This result correlates well with the observed direct (fast) association reaction (eq 3a) which initiates the catalytic CO_2 formation cycle. The binding energy of CO to Au_2^- (in a planar end-on configuration similar to the one described for the oxygen molecule: d(Au−Au) = 2.64 Å, d(Au−C) = 2.04 Å, d(C−O) = 1.19 Å, the angle ∠(Au−C−O) = 132.2° and ∠(Au−Au−C) = 180°) is 0.96 eV, which is in an excellent agreement with a recent photodesorption experiment where a value of 0.91 eV has been measured.[23] The stronger binding of O_2 to Au_2^- explains the observation that high CO partial pressures are required before CO adsorption can compete with O_2 adsorption as the first reaction step. Five structures corresponding to the mass of the complex $Au_2CO_3^-$ were studied, and the pertinent structural and energetic information is given in Figure 6 and Table 3. In the following we discuss the formation and stability of these structures with respect to preformed $Au_2O_2^-$. This analysis leads us to conclude that structures C and D (see Figure 6) are the ones pertinent to the observed reaction steps 3b (equilibrium between CO association to $Au_2O_2^-$ to form $Au_2(CO)O_2^-$, and dissociation of the latter to form $Au_2O_2^-$) and 3c (formation of CO_2).

Structures A and B correspond to molecular co-adsorption of CO and O_2 to Au_2^-. From the two molecularly co-adsorbed species, CO can readily (without barrier) bind to the end of the Au−Au axis (structure A) whereas a barrier of 0.2 eV was found for CO association from the gas phase to the Au−Au bridging site of structure B, where the Au−Au bond is significantly elongated to 3.34 Å. The barrier for forming B from A via displacement of CO from the end of the complex to the Au−Au bridge is rather high (on the order of 0.9 eV). In both structures A and B the O−O bond is activated to a value typical to a superoxo-species (about 1.35 Å). The stability of structure C is close to that of A. It contains a reacted O−O−C−O group that is attached through the carbon atom to the gold dimer anion. The O−O bond is activated to a superoxo-state, and this species bears some resemblance to the gold−peroxyformate complex identified in the early experiments of gold atoms in cryogenic CO/O_2 matrices.[24] We studied the formation of this species (C) via two routes: (i) a Langmuir−Hinshelwood (LH) mechanism that involves migration of the preadsorbed CO from the bridging position in structure B and (ii) an Eley−Rideal (ER) mechanism where CO(g) approaches the preformed $Au_2O_2^-$. The LH mechanism has a high activation barrier of 1.1 eV, and since the barrier is of the order of the activation energy for CO desorption from structure B (1 eV), formation of C from B is unlikely. An alternative LH process leading to the formation of structure C starting from A can also be excluded, since it will involve first a transformation from structure A to that in B, with the latter involving (as aforementioned) a barrier of

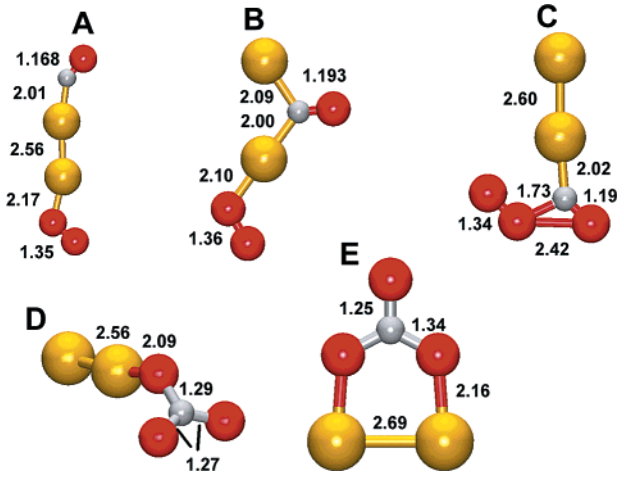

Figure 6. Five optimized structures (A−E) of $Au_2CO_3^-$, with bond lengths in angstroms. The relative stability of these structures is shown in Table 2. A, B, C, and E are planar, and the two carbonate species (D and E) have C_{2v} symmetry. Structures C and D are the ones pertinent for the reactions discussed in the text. Au atoms are depicted by large yellow spheres, a small gray sphere corresponds to the carbon atom, and the oxygen atoms are depicted by red spheres.

Table 3. Stability (ΔE) Relative to the Structure Marked D (a Lower Value Corresponds to a Species of Higher Stability), Vertical Electron Detachment Energy (VDE), Binding Energy (to the Gold Dimer Anion) of CO (BE(CO), with O_2 Preadsorbed) and of O_2 (Be(O_2), with CO Preadsorbed) for the Five Structures (A−E) of $Au_2CO_3^-$ Shown in Figure 6

structure	ΔE (eV)	VDE (eV)	BE(CO) (eV)	BE(O_2) (eV)
A	2.80	2.82	0.93	1.34
B	2.94	3.32	0.78	1.20
C	2.82	3.82	0.91	1.32
D	0	4.67	3.72	4.14
E	1.04	3.38	2.69	3.10

(22) Valden, M.; Lai, X.; Goodman, D. W. *Science* **1998**, *281*, 1647.
(23) Lüttgens, G.; Pontius, N.; Bechthold, P. S.; Neeb, M.; Eberhardt, W. *Phys. Rev. Lett.* **2002**, *88*, 076102.
(24) Huber, H.; McIntosh, D.; Ozin, G. A. *Inorg. Chem.* **1977**, *16*, 975.

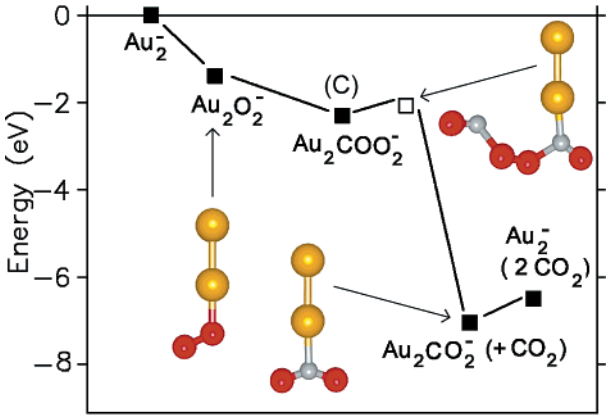

Figure 7. Energetics of the ER mechanism of the reaction, where the peroxyformate-like species $Au_2COO_2^-$ (configuration C in Figure 6) is the metastable intermediate state. The open square denotes the reaction barrier connecting the peroxyformate-like state with the $Au_2CO_2^- + CO_2$ product, and the corresponding transition state configuration is shown at the top right. The last step of the reaction is the desorption of CO_2. The initial energy level at zero corresponds to the sum of the total energies of all the reactants ($Au_2^- + O_2 + 2CO$).

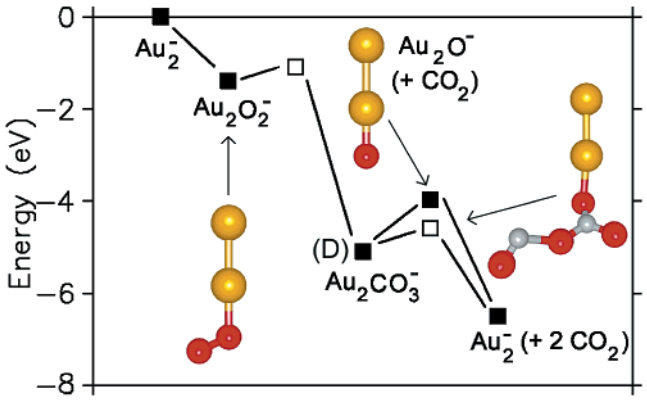

Figure 8. Energetics of the ER mechanism of the reaction where the carbonate species $Au_2CO_3^-$ (configuration D in Figure 6) is the metastable intermediate state. The open squares denote the reaction barriers. The first reaction barrier is associated with the insertion of CO into the O−O bond of $Au_2O_2^-$ (see structure on the left) leading to formation of $Au_2CO_3^-$. Subsequently, two reaction paths are shown. One path involves thermal dissociation of the carbonate to produce Au_2O^- (see the structure shown at the top) which then reacts with CO(g) releasing another CO_2 molecule. The other path proceeds through an ER reaction of the carbonate with CO(g) and it results in the formation of two CO_2 molecules. The latter path involves a barrier of 0.5 eV, and the corresponding transition-state configuration is shown on the right.

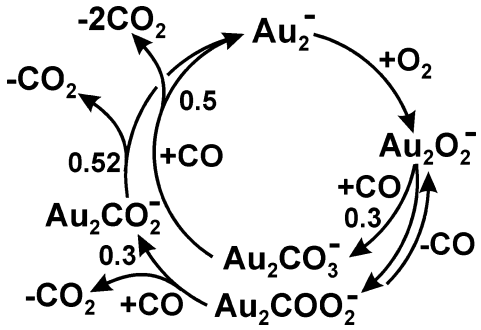

Figure 9. Schematic depiction of the gas-phase catalytic cycle for oxidation of carbon monoxide by gold dimer anions, based on the reaction mechanism determined by kinetic measurements in conjunction with first-principles calculations.

about 0.9 eV (which is close to the binding energy of CO in structure A). Consequently, we conclude that the ER mechanism is the favorable one for the formation of structure C. Interestingly, the ER mechanism (ii) does not involve an activation barrier.

By far the most stable structures corresponding to the mass of $Au_2CO_3^-$ are the two carbonate species D and E. Both structures were discussed by some of us before.[4] Structure E requires a preformed $Au_2O_2^-$ where the molecular axes of Au_2 and O_2 lie parallel to each other. Since this structure of $Au_2O_2^-$ is 1 eV less stable than the ground state discussed above (the binding energy of oxygen in this configuration is 0.39 eV vs the optimal binding energy of 1.39 eV), it is unlikely to be formed and consequently we do not expect structure E to play a relevant role in the catalytic cycle. On the other hand, formation of the most stable structure D by an ER mechanism with the insertion of CO(g) into the O−O bond in $Au_2O_2^-$ (where the O_2 molecule is end-on bonded to the gold dimer anion) requires a barrier of only 0.3 eV, which is easily overcome under our experimental conditions.

The absence of the complex $Au_2C_2O_4^-$ in the experimental mass spectrum, as well as the calculated high barriers for CO migration along the Au−Au axis, suggest an ER mechanism for the final reaction step (eq 3c). It is also worth noting that other intermediates, such as Au_2O^- and $Au_2CO_2^-$, are not observed experimentally. Consequently, two scenarios are suggested for the final reaction step (3c): (i) an ER reaction of CO(g) with structure C (see Figure 6), (ii) an ER reaction of CO(g) with structure D; in both cases the reaction proceeds to completion releasing $2CO_2$ molecules. The energetics of the CO oxidation reaction involving the two mechanisms are shown in Figures 7 and 8, respectively. The formation of CO_2 from the reaction between CO(g) and structure C (scenario (i), Figure 7) involves a low barrier of 0.3 eV (see the transition state configuration in Figure 7), resulting in the formation of a metastable $Au_2CO_2^-$ complex, where CO_2 is bound to Au_2 via the carbon atom (see the structure of this complex in Figure 7). However, the heat of reaction (4.75 eV) evolving from the formation of the first CO_2 molecule is large enough in order to overcome the binding energy (0.52 eV) of the remaining CO_2 to Au_2^-, thus facilitating its desorption from the metal cluster.

The second scenario involves two branches (Figure 8).[4] In the first one, thermal dissociation of CO_2 from the carbonate D (which is endothermic by 1.12 eV) produces a highly reactive species, Au_2O^-, which reacts spontaneously (i.e., without an activation barrier) with CO(g) to produce CO_2. The second branch consists of an ER reaction of CO(g) with species D to produce CO_2. While this step involves a modest barrier of 0.5 eV (denoted by an open square, with the corresponding transition-state configuration shown on the right in Figure 8), it releases readily *two* CO_2 molecules, since the remaining $Au_2CO_2^-$ species, where CO_2 is bound to Au_2 via one of the oxygen atoms, is unstable; under our experimental conditions (100−300 K), this reaction branch is the favorable one.

Summary

In this paper we presented experimental and theoretical evidence for a catalytic cycle of CO oxidation by gas-phase Au_2^- clusters (see Figure 9)

$$Au_2^- + O_2 + 2CO \rightarrow Au_2^- + 2CO_2$$

The experiments consisted of measurements of the kinetics of the reaction in the temperature range of 100 to 300 K in an ion trap setup. A key metastable intermediate with a mass of $Au_2CO_3^-$ was observed. First-principles simulations provided a comprehensive understanding of the energetics and atomic structures of all the reaction intermediates. The theoretically predicted[4] intermediate $Au_2CO_3^-$ was assigned to have two alternative structures (i.e., digold carbonate or peroxyformate-like structures). The peroxyformate-like species can be formed without an activation barrier and is assumed to be able to redesorb CO as observed in the experiment. Both the peroxyformate and carbonate species have low activation barriers (0.3−0.5 eV) for the formation of CO_2, thus facilitating the observed low-temperature catalytic activity of Au_2^-.

Acknowledgment. The theoretical work (H.H and U.L.) was supported by the U.S. Air Force Office for Scientific Research. Computations were performed at the Georgia Tech Center for Computational Materials Science and the National Energy Research Supercomputing Center (NERSC) at the Lawrence Berkeley Laboratory. The experimental work was supported by the Deutsche Forschungsgemeinschaft (SFB 450).

JA027926M